THz spectroscopy on graphene-like materials for bio-compatible devices

Gian Paolo Papari, Valentina Gargiulo, Michela Alfè, Roberto Di Capua, Alessandro Pezzella, and Antonello Andreone

Citation: Journal of Applied Physics **121**, 145107 (2017); doi: 10.1063/1.4980106

View online: https://doi.org/10.1063/1.4980106

View Table of Contents: http://aip.scitation.org/toc/jap/121/14

Published by the American Institute of Physics

THz spectroscopy on graphene-like materials for bio-compatible devices

Gian Paolo Papari,[1,2,a)] Valentina Gargiulo,[3] Michela Alfè,[3] Roberto Di Capua,[1,2] Alessandro Pezzella,[4,5] and Antonello Andreone[1,2]
[1]*Dipartimento di Fisica, Universitá di Napoli "Federico II," via Cinthia, I-80126 Naples, Italy*
[2]*CNR-SPIN, UOS Napoli, via Cinthia, I-80126 Naples, Italy*
[3]*Istituto di Ricerche sulla Combustione (IRC) – CNR, P.le Tecchio 80, I-80125 Naples, Italy*
[4]*Dipartimento di Scienze Chimiche, Università di Napoli "Federico II," Via Cinthia, I-80126 Naples, Italy*
[5]*Istituto per Polimeri, Compositi e Biomateriali (IPCB), CNR, Via Campi Flegrei 34, 80078 Pozzuoli (Na), Italy*

(Received 25 January 2017; accepted 31 March 2017; published online 14 April 2017)

Graphene-like (GL) layers and eumelanin-based graphene-like (EUGL) hybrids have been investigated through THz time domain spectroscopy. The interest in these materials lies on their peculiar chemical-physical properties: the former are conductive water stable materials, whereas the latter are biocompatible materials with good conductive and adhesive properties. Both exhibit promising optoelectronic and bioelectronic applications. We measured mixtures of GL layers or EUGL hybrids with KBr, shaped in pellets with uniform thickness, in order to circumvent problems related to sample inhomogeneity and roughness. A mean field theory was applied to extract direct information on permittivity and conductivity. Data have been carefully fitted through the Drude-Smith theory, confirming the conductive nature of the hybrid materials. The results show that EUGL hybrid-based devices can be promising for the next generation of printable bio-circuits. *Published by AIP Publishing*. [http://dx.doi.org/10.1063/1.4980106]

INTRODUCTION

Graphene represents the first achievement of a fully 2-dimensional material. A single sheet of carbon atoms is technologically versatile for its high ease of integrability[1–4] and fruitful electrodynamic properties in the THz region, where it has been considered for the development of sensors,[5,6] filters,[7] spatial light modulators,[8–10] and mantle cloaks.[11]

Graphene has been hybridized with organic based electronics,[12,13] and it has been extensively used for the production of novel biocompatible devices.[14–16] Within this frame, the possibility to reproducibly fabricate graphene based nanowires and interfaces becomes quite relevant although only few attempts have been made so far.[17]

Recently, a reliable way for the realization of graphene micro-circuitry turned out to be the exploitation of graphene-like (GL) layers.[18,19] A GL layer is a platelet composed of a few layers of graphenic fragments having a width of few nanometers. As a consequence of the manufacturing process, GL layers are produced in water suspension, inherently predisposed to be molded in many shapes, and suitable for wiring organic electronic structures by spraying and/or ink-jet printing techniques either on rigid or flexible supports. An entire set of optical devices, including metamaterials, filters, absorbers, modulators, and cloaks, can be newly proposed through the employment of moldable GL materials. Analogous to some use of carbon nanotubes,[20] GL layers allow further interesting applications to create new and cost-effective materials with tailored electrodynamic properties, for instance, through the mixture with specific insulating,[21] biocompatible,[22] and photoactive[23] components.

Within the scenario of bio-electronics, eumelanin (EU), a proved biocompatible material,[24] can be exploited as an insulating sheath and host for GL layers in bioorganic environments.[22]

In this work both GL layers and biocompatible eumelanin-based graphene-like (EUGL) hybrids have been explored through THz time domain spectroscopy.

THz spectroscopy is a reliable technique to investigate the electrodynamics of any material at high frequencies,[25,26] provided that samples fulfill specific requirements. In particular, in order to avoid any spurious diffractive loss, samples under test have to be homogeneous within the minimum wavelength of the THz signal with a minimum and well-known thickness.[27–30] Indeed, if the sample is too thin, measuring a transmitted or a reflected signal with a poor information content is risky, since it is indistinguishable from the reference one. On the other hand, a thick sample might absorb more signals, leading to a detrimental decrease in the signal-to-noise ratio (SNR).

Any approach to deposit GL layers on a substrate for THz spectroscopy, for instance, using typical techniques such as drop casting or spinning, must therefore take into account the above problems related to large inhomogeneity and/or low absorption.

Good results have been achieved fabricating pellets with a precise control of thickness, obtained by mixing the material (guest) under investigation with appropriate host powder (KBr).

A mean field theory can be subsequently applied for extracting the intrinsic properties of the guest substance.[31] Tuning the concentration of the guest material—be it the GL or the EUGL material—in the KBr powder, we can infer some of its intrinsic electrodynamic parameters (EPs), such as complex permittivity $\tilde{\varepsilon}$ and hence conductivity σ_r.

[a)]papari@fisica.unina.it.

EXPERIMENTAL TECHNIQUES

THz spectroscopy measurements have been performed using a time-domain system based on a fs fiber laser (Menlo Systems). A THz beam is generated and detected through two photoconductive antennas based on GaBiAs semiconductor technology. The beam focus is approximately 2 mm in diameter with a Gaussian profile. Here, we present the results of normal incidence measurements in the band (0.3–2.0) THz. The transmitted electrical field E(t) is sampled at about 0.1 ps in a time interval of 100 ps. A frequency spectrum of the signal is achieved by applying the Fast Fourier Transform (FFT) to the temporal pulse, achieving a resolution of about 0.01 THz. Samples are placed on an aluminum plate provided with circular holes with a diameter of 8 mm, as sketched in Fig. 1(a). The holder is mounted on a two-dimensional motor stage, which enables to acquire measurements through free space, reference, and samples during the same run, with an enhanced accuracy on the phase and amplitude of each single acquisition. In order to reduce or eliminate the effect of H_2O absorption in the frequency spectra, all measurements are performed in a purging box filled with N_2 and a humidity level lower than 1%.

Analytical grade chemicals were purchased from Sigma Aldrich and used without any further purification. CB (N110 type, furnace black, 15–20 nm primary particle diameter, and 139 m^2 g^{-1} specific BET area) was purchased from Sid Richardson Carbon Co.

Synthesis of GL layers

GL layers were obtained applying a two-step oxidation/chemical reduction strategy reported in previous works[18,19] (Fig. 2(a)). A brief description of the applied method is as follows: 500 mg of carbon black (CB) powder was oxidized with nitric acid (67%; 10 mL) at 100 °C under stirring and refluxing for 90 h. The oxidized carbonaceous material, labeled as GL-ox, was recovered by centrifugation and washed with distilled water until acid traces were successfully removed. After the oxidation step, 60 mg of GL-ox was dispersed in distilled water (60 mL) and treated with hydrazine hydrate (1.35 mL) at 100 °C under reflux. After 24 h, the suspension was cooled at room temperature, and the excess of hydrazine was neutralized with a diluted nitric acid (4 M), allowing the precipitation of a black solid: the GL layers. GL layers were recovered by centrifugation (3000 rpm; 30 min), washed with distilled water, and recovered again by centrifugation. This last purification step was repeated twice. The material was in part stored as the aqueous suspension (mass concentration, 1 mg mL^{-1}; pH 3.5) and in part dried at 100 °C and stored.

Synthesis of EU

EU was synthesized under biomimetic conditions through 5,6-dihydroxindole (DHI) and 2-carboxy-5,6-dihydroxindole (DHICA) oxidative co-polymerization[24] (Fig. 2(b)). DHI and DHICA were prepared according to a procedure previously described.[32] A mixture (3:1 in weight) of DHI/DHICA was dissolved in methanol (20 mg mL^{-1}) by ultrasonic agitation, and the resulting suspension was kept under magnetic stirring for 10 min. The pH was adjusted to 8 with ammonia solution (28% in water), allowing indoles to auto-oxidize and polymerize. After 1 h, the reaction was quenched by adding acetic acid solution (1 M) until pH 4 is established. The material was then dried at 100 °C and stored as EU.

Synthesis of EUGL hybrids

The hybrid material EUGL was prepared according to the procedure previously described.[22] Briefly (Fig. 2(c)), an appropriate amount of GL layers in the aqueous suspension (1 mg mL^{-1}) was added to the mixture of EU precursors (DHI/DHICA) in methanol. Then, the ammonia solution was

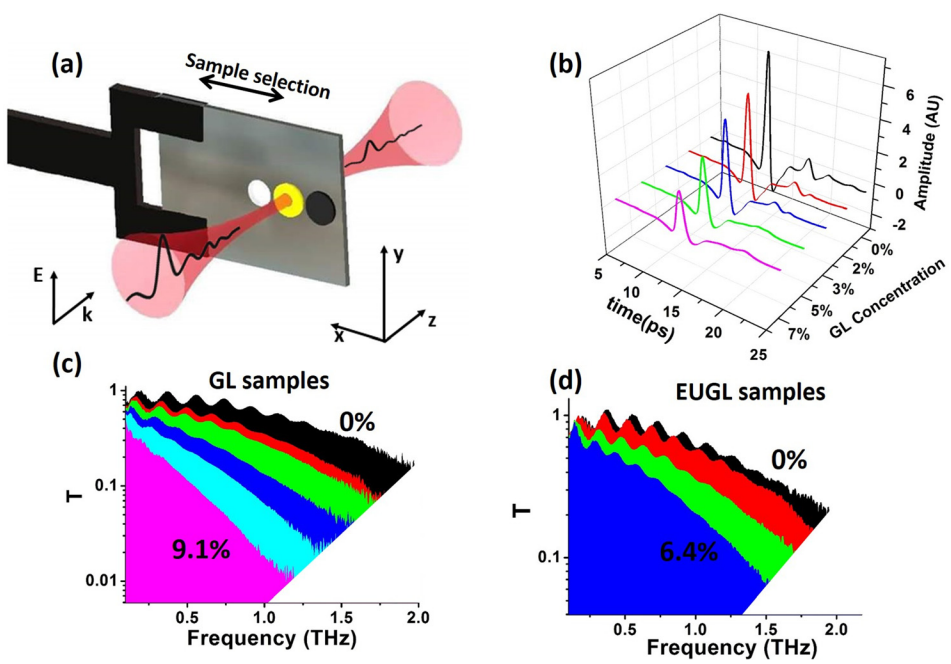

FIG. 1. (a) Schematic representation of the experimental setup. (b) Time dependent evolution of the transmitted THz signal as a function of different GL concentrations (color online). Black: 0% (pure KBr); red: 2%; blue: 2.9%; green: 4.7%; magenta: 6.5%. Graphs (c) and (d) present the THz normalized transmission in the frequency domain through a representative choice of GL and EUGL samples, respectively. Percentages refer to the concentration of GL and EUGL in the pure KBr matrix.

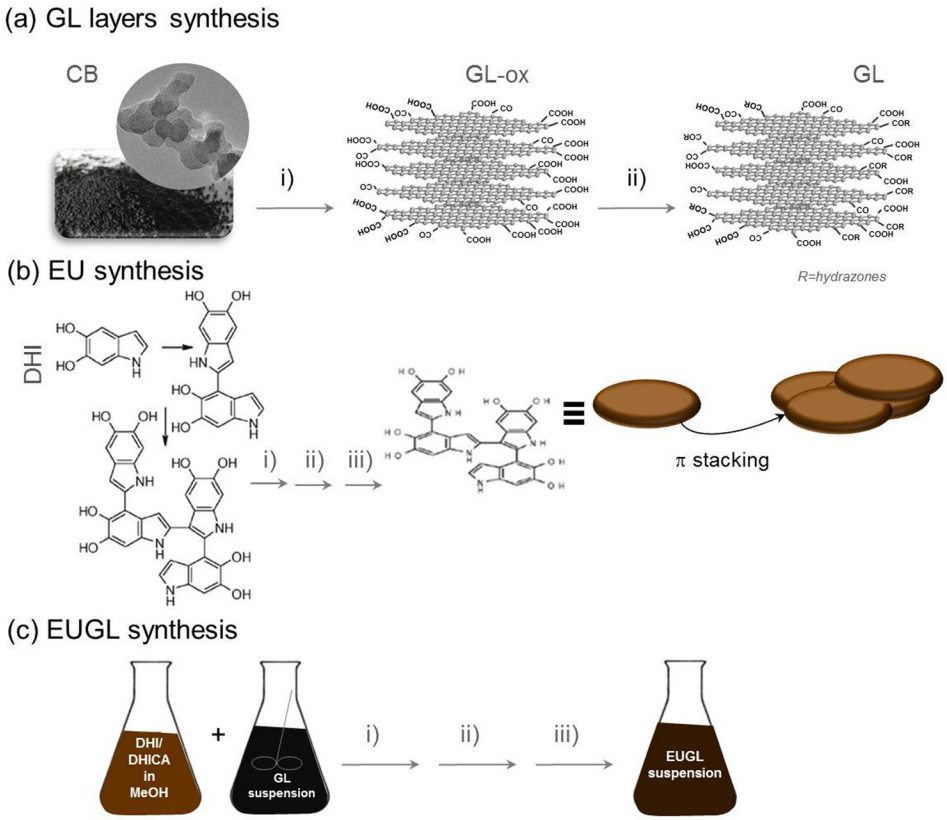

FIG. 2. Materials preparation. GL layers: (i) 100 °C, 90 h/HNO_3; (ii) 100 °C, 24 h, NH_2NH_2 H_2O. EU: (i) DHI+DHICA, 10 min at T room (pH ∼ 4); (ii) NH_3, 30 min at T room (pH ∼ 8); (iii) Acetic acid, 10 min at T room (pH ∼ 4); EUGL: (i) DHI+DHICA +GL layers, 10 min at T room (pH ∼ 4); (ii) NH_3, 30 min at T room (pH ∼ 8); (iii) Acetic acid, 10 min at T room (pH ∼ 4).

added to induce the EU precursors oxidation and polymerization. The mechanism of the reaction was the same as described for the preparation of pure EU. The suspension was dried in an oven at 100 °C and stored. After drying, the EUGL hybrid became insoluble in water.

Materials characteristics

In previous studies, the structural and morphological properties of GL layers, EU, and EUGL were investigated using a large array of instrumental techniques.[18,19,22] The materials relevant properties are summarized below.

During the two-step preparation of GL layers (Fig. 2(a)), the oxidation step destroyed the CB architecture, providing hydrophilic nanoparticles (GL-ox) functionalized with oxygen functional groups (hydroxyl, carboxyl, and carbonyl). The subsequent reduction step (Fig. 2(a)) leads to the production of GL layers[18] bearing residual surface functionalities. Infrared spectroscopy (FTIR), X-ray photoelectron spectroscopy (XPS), and coulometric titrations indicated the presence of carboxyl and carbonyl groups and a minor presence of anhydride or lactone functionalities.[18,19] The acidic functionalities cause the anionic charge of the surface, responsible for the good stability of the GL layers in the aqueous suspension (zeta potential is negative, −45 mV, from pH 3.70 to 14).[19] Raman spectra characteristics of GL-ox and GL layers[18] are consistent with the occurrence of a multilayer structure: D ad G bands have comparable heights and very close values for the D-band to the G-band ratio. These circumstances indicate a significant structural disorder and furnish a clear indication that the oxidation process preserves the graphitic network (also confirmed by UV–visible spectroscopy) and that the chemical functionalization occurs at the edge and not at the basal planes of the GL layers. We thus assume that GL layers consist of water-stable small graphenic fragments composed by 3 or 4 stacked graphene layers decorated at the layer edge with oxygen functional groups.

The copolymerization strategy adopted for EUGL synthesis[22] allowed the entrapment of GL layers into EU structures and allowed the production a hybrid material possessing features that can be considered as the outcome of almost quantitative merging of the parent materials (EU and GL layers). The FTIR spectroscopy data showed the coexistence of the typical signature of both EU and GL layers in the EUGL spectrum and confirmed the actual formation of EU starting from indoles precursors (DHI and DHICA) also in the presence of GL layers. The broadband feature exhibited by the EUGL FTIR spectrum and the higher absorption in the visible region, with respect to pure EU, are indicative of the π-domain growth and of an intimate contact between the components of the hybrid. Although it is not possible to produce conclusive hypothesis for the EU–GL layer interaction, both covalent bonds and $\pi-\pi$ stacking are expected to be involved. Covalent bonds may arise following the attack of nucleophilic units of the GL layers (residual OH groups,[18]) toward electrophilic moieties (quinone and quinonoid systems) of EU precursors. $\pi-\pi$ stacking is expected based on the known tendency of graphene related materials to interact with aromatic systems.

The morphology of EU, GL layer, and EUGL thin films was investigated by Atomic Force Microscopy (AFM) (Fig. 3). GL layers tend to self-assemble in thin films after drying when drop cast forms suspension at pH 3.5/3.7.[18,19,22] In

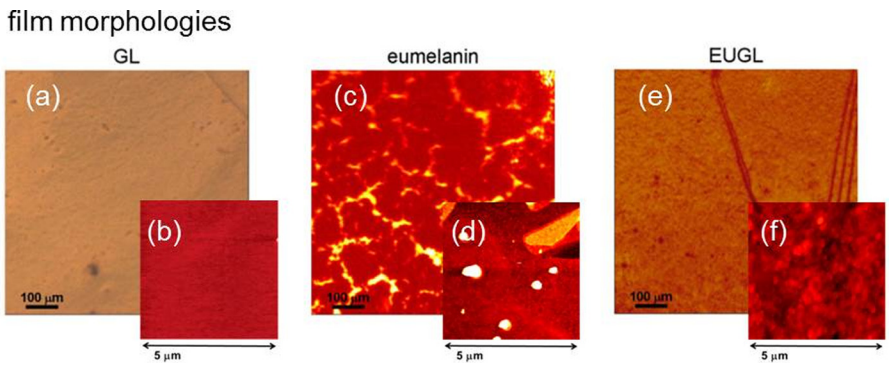

FIG. 3. Optical images of GL (a), EU (c), EUGL (e) film together with non-contact AFM images, (b), (d), (f), respectively (the latter adapted from Ref. 22).

comparison to GL layers, the film morphology of EU and EUGL is clearly modified. While the surface of the neat GL film appeared to be atomically flat over a large area, the EU and EUGL surfaces exhibit a higher roughness, with different general features. Besides the local roughness, the EU surface appeared to be made of larger regions and terraces with different morphologies. EUGL exhibited a locally more granular surface, but the general aspect is much more homogenous, compared to pure EU.[22]

Electrical dc-measurements, realized in a standard four-contact van der Pauw method,[33] revealed that reduced samples (GL layers) exhibited a conducting behavior, with their resistivity being of the order of 1 Ω·m.[18] EU exhibited poor electrical conductivity, confirming its insulating nature; on the other hand, EUGL exhibited an electrical conductivity more than four orders of magnitude greater than parent EU ($\sigma_{EU} = (3.6 \pm 0.5) \times 10^{-8}$ S/cm and $\sigma_{EUGL} = (9 \pm 2) \times 10^{-4}$ S/cm). Moreover, EU and EUGL showed a time-decay of electrical conductivity different from GL, where this phenomenon is absent. The decay of σ takes place, on the two samples, on very different time scales and amounts, being much faster and pronounced in EU than in the hybrid material.[22]

The biocompatibility of EUGL was checked in mammalian cell cultures *in vitro*.[22] EUGL exhibited a wide biocompatibility being not toxic to Murine Embryonic Stem Cells (ESCs) and Rat Microglial Cells (MCs) and bereft of pro-inflammatory potential towards MCs.

Preparation of the pellets

Solid dispersions were prepared by mixing and grinding the materials with KBr (host) in the mass ratios reported in Table I. The solid dispersions were compressed at 10 tons for 10 min into thin disks (pellets; 13 mm in diameter) having thickness values ranging between 380 and 450 μm.

A physical mixture of EU and GL layers was also prepared by simply mixing the two components. The sample named EU+GL was tested in the same conditions of EUGL to prove the effect of the interactions established between the two components during the co-polymerization process. The amounts of EU and GL used to prepare EU+GL were those necessary to achieve a mass ratio between EU and GL of 1:1, as in the sample EUGL_1.

All the samples analyzed in this work and the corresponding labels are listed in Table I.

THEORETICAL BACKGROUND

Frequency dependent electrodynamic properties of the samples under test have been collected by employing a standard approach based on the computation of the transfer $T(\omega)$ function ($\omega = 2\pi f$), experimentally obtained through the ratio between the signal transmitted through the material $E_s(\omega)$ and the signal achieved in air $E_r(\omega)$[30]

$$T(\omega) = \frac{E_S(\omega)}{E_R(\omega)} = \frac{4\tilde{n}_s\tilde{n}_{air}}{(\tilde{n}_s + \tilde{n}_{air})^2}\exp\left[-i(\tilde{n}_s + \tilde{n}_{air})\frac{\omega d}{c}\right] \cdot FP(\omega),$$
$$FP(\omega) = \frac{1}{1 - \left(\frac{\tilde{n}_s - \tilde{n}_{air}}{\tilde{n}_s + \tilde{n}_{air}}\right)^2 \exp\left(-i2\tilde{n}_s\frac{\omega d}{c}\right)}. \quad (1)$$

Here, $\tilde{n}_s$ is the complex refractive index of the sample, $\tilde{n}_{air}$ the refractive index of air, d the sample thickness, and c the speed of light. The function FP accounts for the Fabry-Perot oscillations due to the multiple reflections of the THz wave at the sample boundaries. A commercial software (Teralyzer™) has been used to gather $\tilde{n}_s = n_s + ik_s$ by applying *the total variation technique*,[28–30] which infers n_s, the extinction

TABLE I. Samples characteristics.

Sample name	Material amount mg	KBr amount mg	Mass ratio %	Thickness cm
CB	2.06	100.20	2.01	0.045
GL-ox_1	2.00	100.20	1.96	0.042
GL-ox_2	3.93	94.83	3.98	0.042
GL-ox_3	8.15	95.10	7.89	0.045
GL_1	2.12	103.93	2.00	0.038
GL_2	3.03	100.30	2.93	0.039
GL_3	5.03	100.98	4.74	0.043
GL_4	6.96	100.01	6.51	0.042
GL_5	10.20	102.30	9.07	0.050
EUGL_1	5.12	95.14	5.11	0.040
EUGL_2	10.06	93.09	9.75	0.042
EUGL_3	3.20	104.89	2.96	0.043
EUGL_4	7.00	102.00	6.42	0.044
EU + GL	5.01	95.86	4.97	0.040

coefficient k_s, and the effective optical thickness d_{eff} retrieved in correspondence with the minimum FP oscillations.

The complex dielectric function $\tilde{\varepsilon}_s$ of each mixture is then achieved through simple algebra $\tilde{\varepsilon}_s/\varepsilon_0 = \varepsilon_r + i\varepsilon_i$, where $\varepsilon_r = n_s^2 - k_s^2$. $\varepsilon_i = 2n_s k_s$,[34] and ε_0 is the vacuum permittivity.

According to Refs. 35 and 36, we can define an uncertainty for each couple of functions in ε_r and ε_i relative to a fluctuation of 1 μm of the optimal sample thickness d_{eff}. This reflects into an error of the order of about $\pm 1\%$ for each curve of either GL or EUGL belonging to a specific concentration.

In order to achieve the intrinsic value of the dielectric function related to either GL or EUGL materials, we employed the mean field theory (Landau–Lifshitz–Looyenga model) described in Ref. 31, where the following relation holds

$$\tilde{\varepsilon}_g(\eta_g) = (\tilde{\varepsilon}_s^{1/3} - (1-\eta_g)\cdot\tilde{\varepsilon}_h^{1/3})^3/{\eta_g}^3. \quad (2)$$

Here, $\tilde{\varepsilon}_g$ represents the complex permittivity of the guest substance (GL or EUGL) and η_g its concentration in volume.

η_g can be easily expressed in terms of the weight concentrations α_g and $\alpha_h = 1 - \alpha_g$ and mass densities ρ_g and ρ_h of the guest and host substance, respectively

$$\eta_g = \left(1 + \frac{\rho_g}{\rho_h}\frac{1-\alpha_g}{\alpha_g}\right)^{-1} \quad (3)$$

obtained through $\eta_g + \eta_h = 1$ and $\alpha_g/\alpha_h = \rho_g\eta_g/\rho_h\alpha_h$.

Equation (2) should allow retrieving the same spectroscopic information regardless the guest volume concentration. By the superposition of various experimental curves $\tilde{\varepsilon}_g(\eta_g)$ collected by different guest/host ratios, one can also better infer the effective electrodynamic parameters.

The permittivity and conductivity of the measured materials have been fitted using a conventional Drude-Smith model.[37,38] Complex permittivity can be written as

$$\tilde{\varepsilon}(\omega) = \varepsilon_\infty - \left\{\frac{\omega_p^2}{\omega^2 + i\omega\omega_\tau}\left(1 + c_1\frac{\omega_\tau}{\omega_\tau - i\omega}\right)\right\}, \quad (4)$$

where ε_∞ is the asymptotic value of ε_r, $\omega_p^2 = ne^2/\varepsilon_0 m^*$ is the plasma frequency, and n and m^* are the carrier density and effective mass, respectively, whereas $\omega_\tau = 1/\tau$ is the relaxation frequency. The coefficient c_1 ranges between -1 and 0 and accounts for the portion of localized/backscattered electrons. Once $\tilde{\varepsilon}(\omega)$ has been properly fitted to experimental data in order to get ε_∞, THz conductivity can be simply obtained through the expression

$$\tilde{\sigma}(\omega) = -i[\tilde{\varepsilon}(\omega) - \varepsilon_\infty]\varepsilon_0\omega \quad (5)$$

and from that the dc conductivity σ_{dc} using

$$\sigma_{dc} = (1 + c_1)\omega_p^2\varepsilon_0/\omega_\tau. \quad (6)$$

MEASUREMENTS AND DISCUSSION

A representative selection of experimental curves is reported in Fig. 1(b), where the time dependent electric field signal E(t) is reported for different concentrations of GL layers in the KBr matrix. Ranging from pure KBr to mixtures having up to 6.5% in the GL mass concentration, curves scale down in amplitude and experience a time delay because of losses and dispersion in the material under investigation.

Meaningful information on the EP of samples can be derived from the frequency transmission $T(\omega)$ in the range of 0.1–2.0 THz reported in Figs. 1(c) and 1(d) for GL/KBr and EUGL/KBr mixtures, respectively, at various mass concentrations. Increasing the content of GL and EUGL in KBr, THz losses increase accordingly so that the signal amplitude scales down and is frequency limited by the lower Signal-to-Noise Ratio (SNR). Therefore, in pure KBr, $T(\omega)$ extends to 2 THz, whereas for the highest GL layers concentration (9.1%), a significant signal is observed up to 1.3 THz only.

Using the retrieval procedure detailed in the previous paragraph, we can extract the complex permittivity and the effective thickness of pure KBr and mixed samples of GL and EUGL. Once $\tilde{\varepsilon}_h$, the complex permittivity of the host substance (KBr), and $\tilde{\varepsilon}_s(\alpha_g)$ have been retrieved, $\tilde{\varepsilon}_g(\alpha_g)$ is obtained employing Equations (2) and (3). At 1 THz, we find $\varepsilon_r(KBr) \cong 5$ and $\sigma_r(KBr) \cong 0.4\,\mathrm{S/cm}$, in substantial agreement with results reported in Ref. 39.

We first use THz spectroscopy to capture changes in the evolution of materials, leading to the production of GL and EUGL.

In Figs. 4(a) and 4(b), the real part of the dielectric response function and of the complex conductivity of CB, GL-ox, and GL layers having a nominal weight concentration of about 3% is reported, respectively. Carbon black is the raw material undergoing two steps of the oxidation-reduction method for the production of GL layers.[18,19]

Both graphs show a clear change in ε_r and σ as a consequence of chemical processes occurred. CB exhibits negative values of ε_r at the lowest frequencies, and its conductivity drastically decreases when it undergoes the oxidation process to produce GL-ox. This behavior has been already observed in other carbon-based systems.[40]

Samples containing GL-ox and GL layers instead mostly differ in their conductive properties. The reduction process enhances the conductivity: σ values in GL layer samples are larger than in GL-ox samples by one order of magnitude or more in the frequency range of investigation.

Our hypothesis is that the carboxylic groups during the oxidation process tend to engage GL-ox electrons into new bounds affecting negatively the conductivity of the material, whereas the transformation of COOH groups during the reduction process gives an enhancement almost tenfold of the GL layer conductivity.

THz spectroscopy is then applied to highlight the differences in the electrodynamic behavior of a simple mixture of EU and graphene-like layers (EU + GL) and of the hybrid obtained through their co-polymerization (EUGL).

In Figs. 4(c) and 4(d), representative examples of the real part of the dielectric function ε_r and conductivity σ_r for EU+GL and EUGL are reported, respectively, as a function of frequency. These quantities have been extracted using pellets with 5% mass concentration. Absolute values strongly

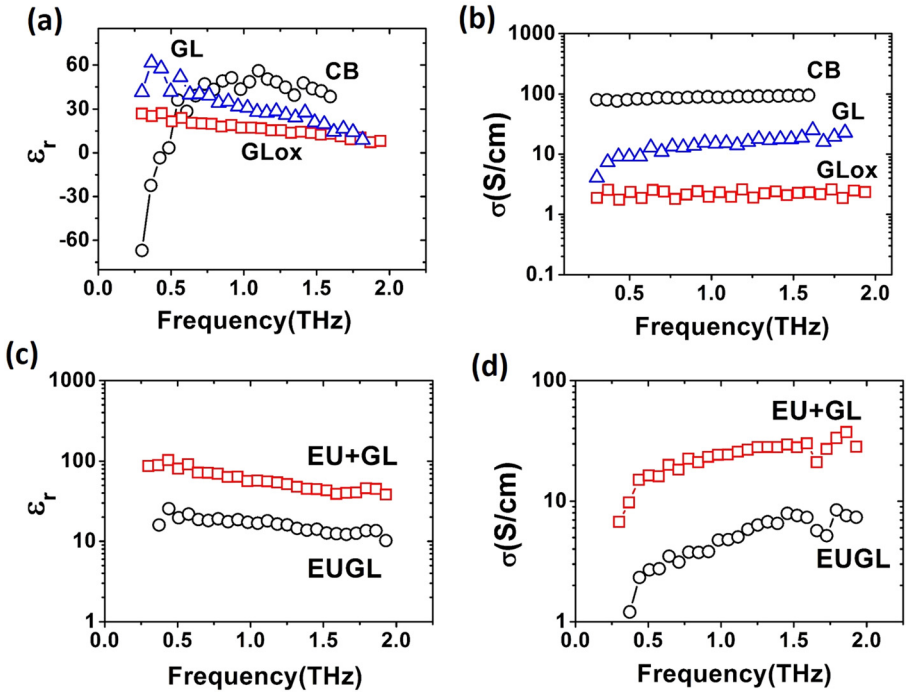

FIG. 4. (a) and (b): frequency dependence of the real part of of dielectric function (ε_r) and conductivity (σ_r), respectively, in a carbon black (CB, black circles), an oxidized graphene-like layers (GL-ox, red squares), and a graphene-like layers (GL, blue triangles) sample. (c) and (d): same quantities compared for a EUGL (black circles) and a EU + GL (red squares) mixture (see text for details).

differ in the two materials; however, they preserve the same frequency dependence.

Polymerization of EU precursors in the presence of GL allows the incorporation of GL layers into EU, giving rise to nanostructures having an average diameter of few tenths of nanometers.[22] This has incisively affected the percolation path when compared to the case of a simple mixture between EU and GL layers. Whether the polymerization triggers the onset of new chemical bonds that may degrade GL conductivity remains an issue that has not been addressed yet.

A summary of the results on the real and imaginary parts of both the dielectric function and the conductivity in different GL and EUGL samples is reported in Figs. 5(a)–5(d). In panels (a) and (b), ε_r and ε_i are plotted as a function of frequency in GL samples, respectively. In panels (c) and (d), the same quantities are shown for EUGL samples.

Among all samples measured, diversified in the guest material and concentration as reported in Table I, only some of them have been selected for the subsequent analysis. When the concentration of the guest material is lower than 2%, the extracted electrodynamic parameters lie outside the "convergence area" reached with higher concentrations. We infer that 2% in weight is the threshold value for triggering percolation, and therefore, all samples below this value have been excluded in the comparison with the theory. In the graphs, for each guest material, a couple of curves with a

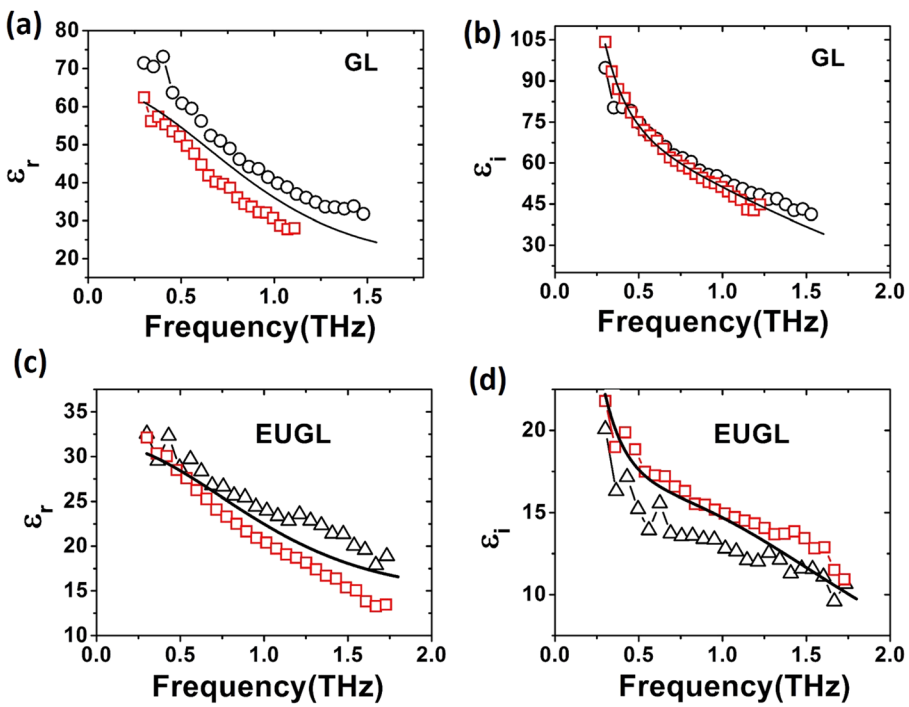

FIG. 5. (a) and (b): frequency dependence of the evaluated real (ε_r) and imaginary part (ε_i) of permittivity for GL samples having two representative mass concentrations: 5% (black circles) and 10% (red squares). (c) and (d): same quantities for EUGL hybrids with two representative concentrations: 3% (black-triangles) and 7% (red squares). Black lines represent the fitting curves obtained using the Drude-Smith model. The best fit aims to run over the average value of $\varepsilon_{r,i}$ between the two bounding curves relative to each couple of GL and EUGL reference concentrations.

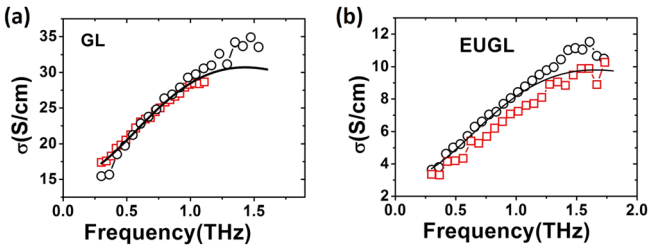

FIG. 6. (a) and (b) show the frequency dependence of the evaluated real part of conductivity for GL and EUGL samples having two representative mass concentrations: 5% (black circles) and 10% (red squares) for GL, 3% (black-triangles) and 7% (red squares) for EUGL. The black line represents the Drude-Smith average trend between each couple of curves.

specific mass concentration have been selected and plotted (for details, see the caption of Fig. 5) to bound the area in ε_r and ε_i vs ω space in a such a way that all other $\tilde{\varepsilon}(\eta_g)$ curves fall inside it. This spread of data, as a function of η_g, defines the uncertainty for electrodynamic parameters achieved through the Drude-Smith model as discussed below. In GL samples, both ε_r and ε_i strongly decrease in the frequency range of 0.3–1.5 THz. In comparison, the hybrid EUGL displays a similar frequency dependence for ε_r, with an average amplitude $|\varepsilon_r(EUGL)| \approx |\varepsilon_r(GL)|/2$. The behavior of ε_i instead is quite different, with nearly a flat frequency dependence and absolute values reduced by a factor 5 or more.

Quantitative insights into the complex dielectric function $\tilde{\varepsilon}$ of both GL and EUGL materials can be retrieved using a simple Drude-Smith model through Eqs. (4) and (5). We found reasonable parameters by fitting *simultaneously* the families of curves $\varepsilon_r(\eta_g)$ and $\varepsilon_i(\eta_g)$ of both GL and EUGL samples. Fitting curves are reported in Figs. 5 and 6 as solid black lines. They nicely reproduce data trends and provide valuable information on the photoconduction. Fitting curves aim to trace the average trend of data, running in between each couple of selected curves. The Drude-Smith model provides the knowledge of 4 parameters for both GL and EUGL, summarized in Table II. Through Equation (6), we can yield the value of the *intrinsic* dc conductivity, whose value is given by $\sigma_{dc} = 15\,\mathrm{S/cm}$ and $\sigma_{dc} = 2.9\,\mathrm{S/cm}$ for GL and EUGL, respectively. The total uncertainty relative to the complex permittivity $(\delta\varepsilon)$ and conductivity $(\delta\sigma)$ is 15% (13%) and 10% (10%) for GL (EUGL) samples. Specifically, the permittivity uncertainty has been calculated by the spread of $\tilde{\varepsilon}$ as a function of concentration η_g so that $\delta\varepsilon = \sqrt{\delta\varepsilon_r{}^2 + \delta\varepsilon_i{}^2}$, whereas $\delta\sigma$ just relies on the data spread detected in the plot of $\sigma_r(\eta_g)$.

GL and EUGL appear sharply different in terms of σ_{dc} and ε_∞ because we find $\sigma_{dc}(\mathrm{GL}) \cong 5\,\sigma_{dc}(\mathrm{EUGL})$ and $1.77\,\varepsilon_\infty(\mathrm{EUGL}) \cong \varepsilon_\infty(\mathrm{GL})$. Also, the values of the plasma frequency ω_p are well separated within the $\delta\varepsilon$ interval, whereas time scales of photoconduction, described by the value of ω_τ, are comparable within the total uncertainty $(\delta\varepsilon)$, because of the dependence of both on conductive properties of GL. Amplitudes of σ_{dc} are suppressed by the factor $1 + c_1$, which limits to less than 30% the fraction of carriers available for direct conduction. GL and EUGL display a conductivity similar to an amorphous carbon,[41] which is a few times lower than those exhibited by carbon nanotube-based[42,43] and a factor 1000 lower than graphene based systems.[42,44] Charge densities of GL and EUGL are factors 10 and 100, respectively, lower than those of carbon nanotubes ($\sim 2.4 \times 10^{19}\mathrm{cm}^3$ (Ref. 41)); indeed, with $n = \omega_p^2 m^* \varepsilon_0 / e^2$, we get $n(GL) \cong 2 \times 10^{18}/\mathrm{cm}^3$ and $n(EUGL) \cong 2 \times 10^{17}/\mathrm{cm}^3$ having employed $m^* = 0.87\,m_e$ the effective charge mass in amorphous carbons.[45] It is interesting to note the presence of a maximum in σ_r for both GL and EUGL at about $f_0 = 1.5$ THz. The same occurrence has been clearly observed at higher frequencies also in carbon nanotube thin films,[43] although a clear explanation has not been provided yet. This maximum is absent in CB and GL-ox samples, possibly because shifted at higher frequencies. The Drude-Smith formula (Eq. (4)) accounts for the onset of a peak in conductivity when $c_1 < -2/3$,[37,46] which embraces our c_1 values. In particular, the maximum in σ_r occurs at the frequency:

$f_0 = \frac{\omega_\tau}{2\pi}\sqrt{3c_1 + 1/c_1 - 1} \approx 2\,\mathrm{THz}$, having used as average parameters $\omega_\tau = 10\,\mathrm{THz}$ and $c_1 = -0.8$. The model cannot distinguish between intra or inter band contributions into the origin of the peak. It basically signals the onset of the fully Drude/metallic like behavior that just decreases as a function of the frequency. Since the peak is absent in the CB sample, we can ascribe the origin of this mechanism to the process underneath the production of both the GL layer and EUGL. The granular composition of both materials can be the key to get insight into the frequency peak position. Following Matthiessen's rule,[47] the Drude-Smith scattering time τ is ascribable to a double channel acting in parallel: $1/\tau = 1/\tau_b + 1/\tau_s$, where τ_b is the bulk relaxation time, whereas τ_s refers to the mean scattering time with grain boundaries, and so, it is related to the grain size. When frequency induces charges to oscillate on an average length smaller than the grain size (d), i.e., on a time scale smaller than τ_s, the scattering process remains substantially dominated by τ_b (indeed $|\sigma|$ for $\omega \gg 2\pi f_0$ becomes Drude like).[47] Experimentally the main size of a grain can be computed $d \cong v_{th}\tau$, where $v_{th} = \sqrt{3k_BT/m^*} \cong 10^5\mathrm{m/s}$ is the thermal velocity and k_B is the Boltzmann constant. Since the maximum in σ_r is placed in correspondence with the threshold between inter-grain $(f < f_0)$ and intra-grain $(f > f_0)$ dynamics, we can assume as a reference scattering time $\tau = 1/f_0$, yielding $d \approx 50\,\mathrm{nm}$, in agreement with AFM images acquired on the pristine material.[18,19]

Our results demonstrate the actual presence of a THz response for both EU and EUGL materials, which can be described inside the general frame of materials properties at very high frequencies. Such materials have already been shown to be highly biocompatible and not producing toxic shards. In addition, we also reported on their easy and scalable fabrication process,[22] as well as the possibility to effectively tune the surface properties and functionalization.[19,22]

TABLE II. List of parameters used for fitting ε_r and σ data through Drude-Smith model. The last two columns account for the total uncertainty relative to $\tilde{\varepsilon}$ and σ_r obtained through data dispersion.

	ε_∞	ω_p (THz)	ω_τ (THz)	c_1	σ_{dc} (S/cm)	$\delta\varepsilon$	$\delta\sigma$
GL	32	83	10	−0.75	15	15%	10%
EUGL	18	50	11	−0.85	3	13%	10%

All the circumstances open the possibility to employ these materials for designing circuits and devices for biocompatible applications and biosensing.

CONCLUSIONS

We have performed a detailed investigation on the high frequency electrodynamics in graphene-like and EU-based graphene-like materials via THz spectroscopy. The materials have been hosted in KBr powder with different concentrations. The intrinsic values of $\tilde{\varepsilon}$ have been achieved through a Landau-Lifshitz approach. Above the percolation concentration, all data converge inside specific areas in $\tilde{\varepsilon}$ vs frequency space, allowing us to get reasonable precision information—using a simple Drude-Smith model—on the electrodynamic parameters of both materials in this frequency range. Measured values of conductivity are encouraging and open the possibility to employ GL and EUGL materials for the development of bio-compatible circuitry and devices working up to the THz range.

[1]G. Liang, X. Hu, X. Yu, Y. Shen, L. H. Li, A. G. Davies, E. H. Linfield, H. K. Liang, Y. Zhang, S. F. Yu, and Q. J. Wang, "Integrated terahertz graphene modulator with 100% modulation depth," ACS Photonics **2**(11), 1559–1566 (2015).

[2]C. J. Docherty and M. B. Johnston, "Terahertz properties of graphene," J. Infrared Millimeter Terahertz Waves **33**(8), 797–815 (2012).

[3]Z. Chen, W. Ren, L. Gao, B. Liu, S. Pei, and H.-M. Cheng, "Three-dimensional flexible and conductive interconnected graphene networks grown by chemical vapour deposition," Nat. Mater. **10**(6), 424–428 (2011).

[4]F. Schwierz, "Graphene transistors," Nat. Nanotechnol. **5**, 487 (2010).

[5]J. Sun, M. Muruganathan, and H. Mizuta, "Room temperature detection of individual molecular physisorption using suspended bilayer graphene," Sci. Adv. **2**(4), e1501518 (2016).

[6]F. Ricciardella, E. Massera, T. Polichetti, M. L. Miglietta, and G. Di Francia, "A calibrated graphene-based chemi-sensor for sub parts-per-million NO_2 detection operating at room temperature," Appl. Phys. Lett. **104**(18), 183502 (2014).

[7]M. Danaeifar, N. Granpayeh, A. Mohammadi, and A. Setayesh, "Graphene-based tunable terahertz and infrared band-pass filter," Appl. Opt. **52**(22), E68–E72 (2013).

[8]B. Sensale-Rodriguez, R. Yan, M. M. Kelly, T. Fang, K. Tahy, W. S. Hwang, D. Jena, L. Liu, and H. G. Xing, "Broadband graphene terahertz modulators enabled by intraband transitions," Nat. Commun. **3**, 780 (2012).

[9]S. H. Lee, M. Choi, T. T. Kim, S. Lee, M. Liu, X. Yin, H. K. Choi, S. S. Lee, C. G. Choi, S. Y. Choi, X. Zhang, and B. Min, "Gate-controlled active graphene metamaterials at terahertz frequencies," in *Proceedings of the Technical Digest 17th Opto-Electronics Communication Conference (OECC)* (2012), Vol. 11, No. 11, pp. 582–583.

[10]N. Kakenov, T. Takan, V. A. Ozkan, O. Balcı, E. O. Polat, H. Altan, and C. Kocabas, "Graphene-enabled electrically controlled terahertz spatial light modulators," Opt. Lett. **40**(9), 1984 (2015).

[11]P. Y. Chen and A. Alù, "Atomically thin surface cloak using graphene monolayers," ACS Nano **5**(7), 5855–5863 (2011).

[12]D. Yoo, J. Kim, and J. H. Kim, "Direct synthesis of highly conductive poly(3,4-ethylenedioxythiophene):Poly(4-styrenesulfonate) (PEDOT:PSS)/graphene composites and their applications in energy harvesting systems," Nano Res. **7**(5), 717–730 (2014).

[13]J. W. Park and J. Jang, "Fabrication of graphene/free-standing nanofibrillar PEDOT/P(VDF-HFP) hybrid device for wearable and sensitive electronic skin application," Carbon N.Y. **87**(C), 275–281 (2015).

[14]T. Cohen-Karni, Q. Qing, Q. Li, Y. Fang, and C. M. Lieber, "Graphene and nanowire transistors for cellular interfaces and electrical recording," Nano Lett. **10**(3), 1098–1102 (2010).

[15]Q. Liu, B. Guo, Z. Rao, B. Zhang, and J. R. Gong, "Strong two-photon-induced fluorescence from photostable, biocompatible nitrogen-doped graphene quantum dots for cellular and deep-tissue imaging," Nano Lett. **13**(6), 2436–2441 (2013).

[16]Q. He, S. Wu, S. Gao, X. Cao, Z. Yin, H. Li, P. Chen, and H. Zhang, "Transparent, flexible, all-reduced graphene oxide thin film transistors," ACS Nano **5**(6), 5038–5044 (2011).

[17]D. Tosic, Z. Markovic, S. Jovanovic, J. Prekodravac, M. Budimir, D. Kepic, I. Holclajtner-Antunovic, M. Dramicanin, and B. Todorovic-Markovic, "Rapid thermal annealing of nickel-carbon nanowires for graphene nanoribbons formation," Synth. Met. **218**, 43–49 (2016).

[18]M. Alfè, V. Gargiulo, R. Di Capua, F. Chiarella, J.-N. Rouzaud, A. Vergara, and A. Ciajolo, "Wet chemical method for making graphene-like films from carbon black," ACS Appl. Mater. Interfaces **4**(9), 4491–4498 (2012).

[19]M. Alfè, V. Gargiulo, and R. Di Capua, "Tuning the surface morphology of self-assembled graphene-like thin films through pH variation," Appl. Surf. Sci. **353**, 628–635 (2015).

[20]R. Casini, G. Papari, A. Andreone, D. Marrazzo, A. Patti, and P. Russo, "Dispersion of carbon nanotubes in melt compounded polypropylene based composites investigated by THz spectroscopy," Opt. Express **23**, 18181–18192 (2015).

[21]M. Alfè, V. Gargiulo, L. Lisi, and R. Di Capua, "Synthesis and characterization of conductive copper-based metal-organic framework/graphene-like composites," Mater. Chem. Phys. **147**(3), 744–750 (2014).

[22]V. Gargiulo, M. Alfè, R. Di Capua, A. R. Togna, V. Cammisotto, S. Fiorito, A. Musto, A. Navarra, S. Parisi, and A. Pezzella, "Supplementing π-systems: Eumelanin and graphene-like integration towards highly conductive materials for the mammalian cell culture bio-interface," J. Mater. Chem. B **3**(25), 5070–5079 (2015).

[23]M. Alfè, D. Spasiano, V. Gargiulo, G. Vitiello, R. Di Capua, and R. Marotta, "TiO_2/graphene-like photocatalysts for selective oxidation of 3-pyridine-methanol to vitamin B3 under UV/solar simulated radiation in aqueous solution at room conditions: The effect of morphology on catalyst performances," Appl. Catal. A Gen. **487**(1), 91–99 (2014).

[24]M. D'Ischia, K. Wakamatsu, A. Napolitano, S. Briganti, J. C. Garcia-Borron, D. Kovacs, P. Meredith, A. Pezzella, M. Picardo, T. Sarna, J. D. Simon, and S. Ito, "Melanins and melanogenesis: Methods, standards, protocols," Pigment Cell Melanoma Res. **26**(5), 616–633 (2013).

[25]M. Hangyo, "Development and future prospects of terahertz technology," Jpn. J. Appl. Phys., Part 1 **54**(12), 120101 (2015).

[26]W. Withayachumnankul and M. Naftaly, "Fundamentals of measurement in terahertz time-domain spectroscopy," J. Infrared Millimeter Terahertz Waves **35**(8), 610–637 (2014).

[27]W. Withayachumnankul, B. M. Fischer, and D. Abbott, "Material thickness optimization for transmission-mode terahertz time-domain spectroscopy," Opt. Express **16**(10), 7382–7396 (2008).

[28]M. Scheller, C. Jansen, and M. Koch, "Analyzing sub-100-μm samples with transmission terahertz time domain spectroscopy," Opt. Commun. **282**(7), 1304–1306 (2009).

[29]T. D. Dorney, R. G. Baraniuk, and D. M. Mittleman, "Material parameter estimation with terahertz time-domain spectroscopy," J. Opt. Soc. Am. A **18**(7), 1562–1571 (2001).

[30]L. Duvillaret, F. Garet, and J.-L. L. Coutaz, "A reliable method for extraction of material parameters in terahertz time-domain spectroscopy," IEEE J. Sel. Top. Quantum Electron. **2**(3), 739–746 (1996).

[31]G. Banhegyi, "Numerical analysis of complex dielectric mixture formulae," Colloid Polym. Sci. **266**, 11–28 (1988).

[32]R. Edge, M. D'Ischia, E. J. Land, A. Napolitano, S. Navaratnam, L. Panzella, A. Pezzella, C. A. Ramsden, and P. A. Riley, "Dopaquinone redox exchange with dihydroxyindole and dihydroxyindole carboxylic acid," Pigment Cell Res. **19**(5), 443–450 (2006).

[33]L. J. van der Pauw, "A method of measuring the resistivity and Hall coefficient on lamellae of arbitrary shape," Philips Tech. Rev. **20**, 220–224 (1958).

[34]L. Angrisani, G. Cavallo, A. Liccardo, G. Papari, and A. Andreone, "THz measurement systems," in *New Trends and Developments in Metrology*, edited by L. Cocco (InTech, 2016).

[35]K. I. Zaytsev, A. A. Gavdush, V. E. Karasik, V. I. Alekhnovich, P. A. Nosov, V. A. Lazarev, I. V. Reshetov, and S. O. Yurchenko, "Accuracy of sample material parameters reconstruction using terahertz pulsed spectroscopy," J. Appl. Phys. **115**(19), 193105 (2014).

[36]I. Pupeza, R. Wilk, and M. Koch, "Highly accurate optical material parameter determination with THz time-domain spectroscopy," Opt. Express **15**(7), 4335–4350 (2007).

[37]N. V. Smith, "Classical generalization of the Drude formula for the optical conductivity," Phys. Rev. B **64**(15), 155106 (2001).

[38]R. Lovrinčić and A. Pucci, "Infrared optical properties of chromium nanoscale films with a phase transition," Phys. Rev. B **80**(20), 205404 (2009).
[39]F. D. J. Brunner, A. Schneider, and P. Gunter, "A terahertz time-domain spectrometer for simultaneous transmission and reflection measurements at normal incidence," Opt. Express **17**(23), 20684 (2009).
[40]X. Yao, X. Kou, and J. Qiu, "Multi-walled carbon nanotubes/polyaniline composites with negative permittivity and negative permeability," Carbon N.Y. **107**, 261–267 (2016).
[41]H. Wang, J. Q. Guo, and Y. S. Zhou, "Understanding terahertz optical properties of amorphous carbon thin films," Carbon N.Y. **64**, 67–71 (2013).
[42]E. Dadrasnia, H. Lamela, M. B. Kuppam, F. Garet, and J.-L. Coutaz, "Determination of the DC electrical conductivity of multiwalled carbon nanotube films and graphene layers from noncontact time-domain terahertz measurements," Adv. Condens. Matter Phys. **2014**, 1–6.
[43]A. M. Nemilentsau, M. V. Shuba, P. N. D'yachkov, G. Y. A. Slepyan, P. P. Kuzhir, and S. A. Maksimenko, "Electromagnetic response of the composites containing chemically modified carbon nanotubes," J. Phys. Conf. Ser. **248**(1), 12003 (2010).
[44]B. Marinho, M. Ghislandi, E. Tkalya, C. E. Koning, and G. de With, "Electrical conductivity of compacts of graphene, multi-wall carbon nanotubes, carbon black, and graphite powder," Powder Technol. **221**, 351–358 (2012).
[45]J. T. Titantah and D. Lamoen, "Determination of the electron effective band mass in amorphous carbon from density-functional theory calculations," Phys. Rev. B **70**(3), 033101 (2004).
[46]J. Lloyd-Hughes and T. I. Jeon, "A review of the terahertz conductivity of bulk and nano-materials," J. Infrared Millimeter Terahertz Waves **33**(9), 871–925 (2012).
[47]H. Němec, P. Kužel, and V. Sundström, "Far-infrared response of free charge carriers localized in semiconductor nanoparticles," Phys. Rev. B **79**(11), 115309 (2009).